Review article

Inelastic electron tunneling spectroscopy by STM of phonons at solid surfaces and interfaces

Emi Minamitani[a,h,*], Noriaki Takagi[b], Ryuichi Arafune[c], Thomas Frederiksen[d,e], Tadahiro Komeda[f], Hiromu Ueba[g,1], Satoshi Watanabe[a]

[a] *Department of Materials Engineering, The University of Tokyo, 7-3-1 Hongo, Bunkyo-ku, Tokyo 113-8656, Japan*
[b] *Gratuate School of Human and Environmental Studies, Faculty of Integrated Human Science, Kyoto University, Yoshida, Kyoto 606-8501, Japan*
[c] *International Center for Materials Nanoarchitectonics (WPI-MANA), National Institute for Materials Science, 1-1 Namiki, Tsukuba, Ibaraki 304-0044, Japan*
[d] *Donostia International Physics Center, Paseo Manuel de Lardizabal, 4, E-20018 Donostia-San Sebastián, Spain*
[e] *IKERBASQUE, Basque Foundation for Science, E-48013 Bilbao, Spain*
[f] *Institute of Multidisciplinary Research for Advanced Materials, Tohoku University, 2-1-1 Katahira, Aobaku, Sendai, Miyagi 980-8577, Japan*
[g] *Division of Nano and New Functional Materials Science, Graduate School of Science and Engineering, University of Toyama, Toyama 930-855, Japan*
[h] *JST PRESTO, 7-3-1 Hongo, Bunkyo-ku, Tokyo 113-8656, Japan*

A B S T R A C T

Inelastic electron tunneling spectroscopy (IETS) combined with scanning tunneling microscopy (STM) allows the acquisition of vibrational signals at surfaces. In STM-IETS, a tunneling electron may excite a vibration, and opens an inelastic channel in parallel with the elastic one, giving rise to a change in conductivity of the STM junction. Until recently, the application of STM-IETS was limited to the localized vibrations of single atoms and molecules adsorbed on surfaces. The theory of the STM-IETS spectrum in such cases has been established. For the collective lattice dynamics, i.e., phonons, however, features of STM-IETS spectrum have not been understood well, though in principle STM-IETS should also be capable of detecting phonons. In this review, we present STM-IETS investigations for surface and interface phonons and provide a theoretical analysis. We take surface phonons on Cu(1 1 0) and interfacial phonons relevant to graphene on SiC substrate as illustrative examples. In the former, we provide a theoretical formalism about the inelastic phonon excitations by tunneling electrons based on the nonequilibrium Green's function (NEGF) technique applied to a model Hamiltonian constructed in momentum space for both electrons and phonons. In the latter case, we discuss the experimentally observed spatial dependence of the STM-IETS spectrum and link it to local excitations of interfacial phonons based on *ab-initio* STM-IETS simulation.

1. Introduction

Phonons, the quanta of collective atom vibrations in periodic lattices, play an important role in condensed matter physics [1,2]. Physical phenomena relevant to phonons are too many to enumerate. For example, the electron transport in condensed matter relies upon not only the electronic band structure near the Fermi level but also the energy and momentum relaxation of conduction electrons by phonon scattering. Strong electron-phonon coupling (EPC) causes distortion of the lattice structure to form a polaron state and it gives rise to phase transitions, such as the Peierls transition and/or charge density wave (CDW). In certain metals, EPC generates pairs of electrons that may condense into a superconducting state. Furthermore, phonons govern the thermal transport in insulators and semiconductors. Uncovering phonon properties relevant to these phenomena is one of the central issues in condensed matter physics. Consequently, various experimental and theoretical techniques have been developed.

Surfaces provides unique platforms to investigate the basic aspects of phonons by means of various spectroscopic techniques. Most surface-phonon spectroscopies correlate their signal with the energy-loss process during incident particle or photon scattering. Representative methods are high-resolution electron energy loss spectroscopy (HREELS) [3], helium atom scattering (HAS) [4,5] and Raman scattering [6]. Surface phonons have been intensively measured by these techniques, and much knowledge has been accumulated. The measured spectra typically provide ensemble averages over macroscopic sample areas. Currently, surface-phonon spectroscopy with atomic-scale resolution is in high demand. Revealing the correlation of lattice dynamical properties with local geometric and electronic structures at clean, reconstructed and molecule-adsorbed surfaces would lead to a deeper understanding of phonon-related phenomena and possibly to tailoring of the functionalities of surface nanostructures. The recent boost in research on atom-layered materials such as graphene [7], X-enes (X = Si, Ge, Sn, and so on) [8–11], and transition metal dichalcogenides (TMDCs) [12,13] makes it highly desirable to acquire insights on the microscopic relations of their electronic and optical properties with the surface and local phonons.

Scanning tunneling microscopy (STM) enables the observation of surface structure and electronic states with atomic-scale spatial resolution. With the advent of low-temperature, ultra-high vacuum STM equipment and inelastic tunneling electron spectroscopy (IETS), the energy loss of tunneling electrons through vibration excitations has become measurable at a single-atom/molecule level [14]. As schematically shown in Fig. 1, the tunneling current I increases linearly as a function of sample voltage V and it further increases when V exceeds a threshold voltage corresponding to the energy of a phonon mode. Here, an inelastic transport channel opens via the excitation of a phonon mode by tunneling electrons, and both elastic and inelastic channels carry I, thereby causing the conductance increase. This appears as a pair of steps in the differential conductance dI/dV and as a peak-and-dip pair in the second derivative d^2I/dV^2 at the phonon energy. Note that d^2I/dV^2 (or its normalized quantity with respect to dI/dV) is commonly denoted as the STM-IETS spectrum. STM-IETS was originally applied to detect the vibrational fingerprint of a single molecule. The earliest example is a single acetylene molecule adsorbed on a Cu(1 0 0) surface [14]. This study triggered the applications of STM-IETS to various molecular adsorption systems [15–17]. Later, STM-IETS was also applied to observe chemical reactions induced by tunneling electrons and developed into a new spectroscopy for adsorbate dynamics induced by vibrational excitations, i.e., action spectroscopy at the single-molecule level [18–21].

In parallel with the experimental studies, theories for STM-IETS have been developed. The possibility of detecting a single-molecule vibration with STM-IETS was discussed before the first successful STM-IETS experiment. Binnig et al. pointed out that molecular vibrations can be observed through the inelastic process in which the tunneling electron interacts with the dipole field induced by vibrational motion [22]. Persson and Baratoff developed a theory based on a resonant scattering model mediated by a negatively-charged molecule [23,24]. When an electron tunnels between the STM tip and a metal substrate through a molecule, the electron is trapped transiently in a molecular orbital and the molecule is negatively charged. The molecular structure evolves to a new equilibrium one for the negatively-charged state and if the structural deformation is significant, vibrationally-excited states are left behind after the electron departs to the substrate with the molecule returning to the initial neutral state. This model is widely accepted as the basic excitation mechanism in vibrational STM-IETS [23,24].

After the first experimental proof, STM-IETS experiments were carried out on various molecular adsorbed systems. They revealed that the spectral intensity strongly depends on the vibrational mode and only a limited set of vibrational modes are observable. This led to a search to find the underlying selection rules to determine the active vibrational modes. Lorente et al. and Mingo et al. discussed selection rules by calculating the transition matrix elements of the potential deformations caused by molecular vibrations [25,26]. The transition matrix element can be written as $|\langle \psi_f | \delta v | \psi_i \rangle|^2$ where $\langle \psi_f |$ and $|\psi_i \rangle$ are the final and initial states associated with
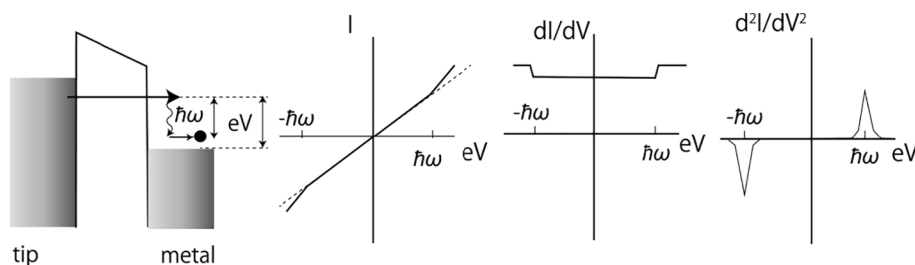

Fig. 1. Schematics of dI/dV (STS) and d^2I/dV^2 (IETS) spectra for an excitation of a phonon with an energy quantum of $\hbar\omega$.

the transition, respectively, and $\delta\nu = \sqrt{\frac{\hbar}{2M\omega}} \frac{\partial\nu}{\partial Q}$, is the deformation potential for the displacement induced by the vibration. Here ν is the single electron potential, M is the reduced mass, Q is the coordinate of the vibration, and $\hbar\omega$ is the energy of the vibrational mode. With the aid of density functional theory (DFT) calculations, the transition matrix formalism enables us to evaluate the transition probability of each vibrational excitation quantitatively. Interestingly, although this formalism does not explicitly include the negatively-charged molecular state, the calculated change in dI/dV can neatly explain the experimental results. By further combination with the nonequilibrium Green's function (NEGF) method, which is a popular technique to treat quantum electronic transport [27–30], we can directly simulate the tunneling current I, dI/dV, and d^2I/dV^2 in realistic systems. The high reproducibility and prediction ability of this technique bring us to the stage in which STM-IETS is established as a single-molecule spectroscopy [31–33].

Although STM-IETS studies have been performed intensively for single molecules, there are only few reports on the application of STM-IETS to surface and interfacial phonons. Revealing the inelastic signals from these should open up a new avenue of STM-IETS to study phonon-related solid-state physics.

In this review, we first briefly describe some previous efforts towards STM-IETS of phonons on a metallic surface. Second, we introduce our theoretical formalism on phonon excitation with STM-IETS for a metallic surface, and show that STM-IETS measures the momentum-resolved Eliashberg function rather than the phonon density of states (phonon DOS). We demonstrate that our formalism describes well the STM-IETS signal derived from a surface phonon on Cu(1 1 0) in combination with the DFT calculations of EPC [34]. Third, we introduce an example of detecting interfacial phonons with STM-IETS, namely, localized phonons at the interface in between graphene and SiC [35]. We show that the experimental STM-IETS spectra taken on graphene-covered SiC are well reproduced using a computational method similar to the molecular system. Finally, we provide a short summary and some perspectives.

2. STM-IETS for solid surfaces

In principle, STM-IETS can detect phonons on solid surfaces. Indeed, phonon features have been observed and reported by STM-IETS for highly ordered pyrolytic graphite (HOPG) [36], Au(1 1 1) and Cu(1 1 1) [37] and Pb islands on Cu(1 1 1) [38]. Unlike molecular vibrations characterized with discrete vibrational levels, phonons have a broad DOS spectrum reflecting their continuous energy dispersions. Thus, it is an open question how the STM-IETS spectrum arising from the excitations of phonons should be analyzed. Although the peaks in the IETS spectrum of HOPG have been assigned to the singular features in the phonon DOS derived from the flat dispersions [36], such straightforward assignments are not valid for Au(1 1 1) and Cu(1 1 1) [37]. Very recently, Schackert et al. showed that the STM-IETS spectra for Pb islands on Cu(1 1 1) are described by the Eliashberg function which is defined by the product of energy-dependent EPC and phonon DOS [38]. As demonstrated in this section, we have developed a theory of the surface phonon excitation by tunneling electrons and show that the STM-IETS spectrum is proportional to the momentum-resolved Eliashberg function. This interpretation of STM-IETS spectra enables us to quantitatively evaluate EPC, which is normally difficult to access.

2.1. Theoretical formulation of STM-IETS spectrum for metal surfaces

Here we introduce a theoretical formulation of STM-IETS to describe the relevance of the Eliashberg function to the inelastic tunneling current, which is applicable to phonon excitations on metallic surfaces. First, we must figure out what kind of processes are responsible for the inelastic current in a STM-IETS measurement. Consider the electron tunneling between an STM tip and a metallic substrate. With a small positive bias, an electron tunnels from a filled state of the STM tip to an empty state of the substrate within the bias window. After the tunneling event, the electron propagates with relaxation of the surplus energy by creating phonons in the substrate. These inelastic processes induced by EPC in the substrate lead to the inelastic signal in the tunneling current.

To evaluate the tunneling current, we use the following Hamiltonian that describes the interactions between an STM tip, substrate conduction electrons, and phonons in the substrate:

$$H = \sum_p \varepsilon_p c_p^\dagger c_p + \sum_{k,\eta} \varepsilon_k^\eta c_{k\eta}^\dagger c_{k\eta} + \sum_{q\lambda} \hbar\omega_q^\lambda a_{q\lambda}^\dagger a_{q\lambda} + \sum_{p,k,\eta} W_{pk}^\eta (c_p^\dagger c_{k\eta} + h.c.) + \sum_{k,p,\lambda,\eta,\eta'} M_{kq}^{\eta'\eta\lambda} c_{k+q\eta'}^\dagger c_{k\eta} (a_{q\lambda} + a_{-q\lambda}^\dagger).$$

(1)

Here p, λ, and η are the indices of the eigenstate of the tip, phonons, and band of conduction electrons, respectively. k and q specify the wave vectors of the conduction electron and phonon, respectively. c_p, $c_{k\eta}$, and $a_{q\lambda}$ are the annihilation operators for electrons in the tip state, conduction electrons, and substrate phonons, and whose energies are ε_p, ε_k^η and $\hbar\omega_q^\lambda$, respectively. W_{pk}^η is the substrate-tip tunneling matrix element, and $M_{kq}^{\eta'\eta\lambda}$ is the EPC matrix element. Because we focus on tip-independent inelastic processes, we ignore the phonons at the tip. (We note that, in general, the tip phonon can affect the IETS spectrum.)

The tunneling current can be calculated from the time derivative of the occupation number at the tip:

$$
\begin{aligned}
I &= 2\frac{\partial}{\partial t} e \sum_p c_p^\dagger(t) c_p(t) \\
&= \frac{2e}{\hbar} \sum_{pk\eta} (W_{pk}^\eta G_{kp\eta}^<(t,t) - W_{kp}^\eta G_{pk\eta}^<(t,t)) \\
&= -\frac{4e}{\hbar} \Re \int d\omega \sum_{pk\eta} W_{kp}^\eta G_{pk\eta}^<(\omega),
\end{aligned}
$$

(2)

where the factor 2 accounts for the spin degrees of freedom and $G_{ij}^<(t, t') = i\langle c_j^\dagger(t') c_i(t)\rangle$ is the lesser Green's function [2,39] and the subscripts i, j = k or p, which correspond to the substrate or tip electron, respectively. From the equation of motion, we obtain $G_{pk\eta}(\omega) = G_{pp}^0(\omega) W_{pk}^\eta G_{k\eta k\eta}(\omega)$ where $G_{pp}^0(\omega)$ is the unperturbed Green's function of the tip electron. Using the Langreth theorem [39], we rewrite the tunneling current from Eq. (2) as

$$I = -\frac{4e}{\hbar} \Re \int d\omega \sum_{pk\eta} W_{kp}^\eta W_{pk}^\eta (G_{pp}^{0r}(\omega) G_{k\eta k\eta}^<(\omega) + G_{pp}^{0\,<}(\omega) G_{k\eta k\eta}^a(\omega)). \tag{3}$$

The superscripts of the Green's function, a and r in Eq. (3), denote the advanced and retarded Green's function, respectively. Within the typical bias voltages applied in the STM-IETS experiments, the electronic properties of both substrate and tip are not significantly perturbed from their equilibrium ones. Under this condition, the tunneling current is approximated as

$$I = \frac{8\pi e}{\hbar} \int d\omega \sum_{pk\eta} W_{kp}^\eta W_{pk}^\eta (f(\omega) - f(\omega - eV)) \rho_p \Im G_{k\eta k\eta}^r(\omega). \tag{4}$$

where ρ_p is the DOS at the STM tip. If ρ_p and W_{pk}^η are constant with respect to the bias voltage, we obtain the following formula of the STM-IETS spectrum.

$$\frac{d^2 I}{dV^2} = -\frac{8\pi e^3}{\hbar} \sum_{pk\eta} |W_{pk}^\eta|^2 \rho_p \left. \left| \frac{\partial}{\partial \omega} \Im G_{k\eta k\eta}^r(\omega) \right| \right|_{\omega=eV}. \tag{5}$$

The effect of EPC is included in the retarded Green's function of the substrate conduction electron, $G_{k\eta k\eta}^r(\omega)$. To the second order in the electron-phonon interaction, $G_{k\eta k\eta}^r(\omega)$ is approximated as

$$G_{k\eta k\eta}^r(\omega) \sim G_{k\eta k\eta}^{0r}(\omega) + G_{k\eta k\eta}^{0r}(\omega) \Sigma^r(k, \eta, \omega) G_{k\eta k\eta}^{0r}(\omega) \tag{6}$$

where $G_{k\eta k\eta}^{0r}(\omega)$ is the unperturbed Green's function and

$$\Sigma^r(k, \eta, \omega) = \sum_{\eta', q, \lambda} |M_{k-qq}^{\eta'\eta\lambda}|^2 \left(\frac{N_{q\lambda} - f(\varepsilon_{k-q}^{\eta'}) + 1}{\omega - \omega_q^\lambda - \varepsilon_{k-q}^{\eta'} + i\delta} + \frac{N_{q\lambda} + f(\varepsilon_{k-q}^{\eta'})}{\omega + \omega_q^\lambda - \varepsilon_{k-q}^{\eta'} + i\delta} \right) \tag{7}$$

is the electron self-energy.

The relation between the IETS spectrum and the Eliashberg function becomes more explicit by restricting the ranges of k and q. In the spherical tip approximation, W_{pk}^η becomes maximum at $k_{||} = 0$ so that the tunneling occurs mainly through the electronic states at the $\bar{\Gamma}$ point in the reciprocal space. This is generally valid for metal surfaces whose electronic band structures have no projection gap at the $\bar{\Gamma}$ ($k = 0$) point. In this sense, our theory is not applied to Cu(1 1 1) and Au(1 1 1) which have a gap at the $\bar{\Gamma}$ point. More generalized calculations are desired for understanding the STM-IETS spectra of Cu(1 1 1) and Au(1 1 1). The range of q can be limited by the phonon dispersions that the low-energy phonons are usually distributed only around the $\bar{\Gamma}$ point. These permit us to consider only $k = q = 0$ when consider the STM-IETS spectrum in the low-bias region within several meV. For higher-bias region, this approximation is too simple to capture the actual inelastic process via the scattering of electrons by phonons with finite k and q. Assuming that the DOS of the conduction electron of band index η at the $\bar{\Gamma}$ point, $\rho_{\bar{\Gamma}}^\eta$, remains unchanged within the range of low applied voltages and takes $\rho_{\bar{\Gamma}}^\eta = \rho_{\bar{\Gamma}}^\eta(E_F = 0) = \delta(E_F - \varepsilon_{\bar{\Gamma}}^\eta)$, then Eq. (5) is rewritten as

$$\frac{d^2 I}{dV^2} = \sum_{\lambda\eta\eta'} \pi^3 |M_{\bar{\Gamma}\bar{\Gamma}}^{\eta'\eta\lambda}|^2 \delta(E_F - \varepsilon_{\bar{\Gamma}}^\eta)^2 \delta(E_F - \varepsilon_{\bar{\Gamma}}^{\eta'}) \{\delta(eV - \omega_{\bar{\Gamma}}^\lambda) - \delta(-eV - \omega_{\bar{\Gamma}}^\lambda)\}. \tag{8}$$

One can see that Eq. (8) resembles the Eliashberg function $\alpha^2 F(\omega)$, which is defined as

$$\alpha^2 F(\omega) = \frac{1}{2\pi\rho(E_F)} \sum_{k,q,\lambda,\eta,\eta'} \frac{2\pi}{\hbar} |M_{k-qq}^{\eta'\eta\lambda}|^2 \delta(E_F - \varepsilon_k^\eta) \delta(E_F - \varepsilon_{k-q}^{\eta'}) \delta(\omega - \omega_{\lambda q}). \tag{9}$$

Here, $\rho(E_F)$ is the DOS of the conduction electron at the Fermi level. This leads us to conclude that the STM-IETS spectrum of a metal surface is proportional to the momentum-resolved Eliashberg function,

$$\alpha^2 F(\omega, k = q = 0) = \sum_{\lambda\eta\eta'} |M_{\bar{\Gamma}\bar{\Gamma}}^{\eta'\eta\lambda}|^2 \delta(E_F - \varepsilon_{\bar{\Gamma}}^\eta) \delta(E_F - \varepsilon_{\bar{\Gamma}}^{\eta'}) \delta(eV - \omega_{\bar{\Gamma}}^\lambda) \tag{10}$$

2.2. Application to the surface phonon excitation on Cu(1 1 0)

We apply Eq. (10) to the STM-IETS spectrum of Cu(1 1 0). Fig. 2(a) shows a typical STM image of Cu(1 1 0) with a low coverage of CO molecules. One can see a homogeneous and flat area together with a small number of adsorbed CO molecules. The CO molecules appear as the dark depressions, indicating the lower DOS available to the electron tunneling. Fig. 2(b) shows an IETS spectrum measured at a clean surface area. A peak-dip pair appears at ± 6 mV. In contrast, the spectrum of a CO molecule (Fig. 2(c)) shows two peak-dip pairs at 6 (−6) and 36 (−36) mV, respectively. The energy positions of these peak-dip pairs match with those of vibrations of CO on metallic surfaces [40–42]. The pair at ± 36 mV is assigned to be the frustrated rotation (FR) of the adsorbed CO molecule [40]. The most plausible origin of lower-energy peak-dip pair is the frustrated translation (FT) mode. Since the energy of 6 meV is
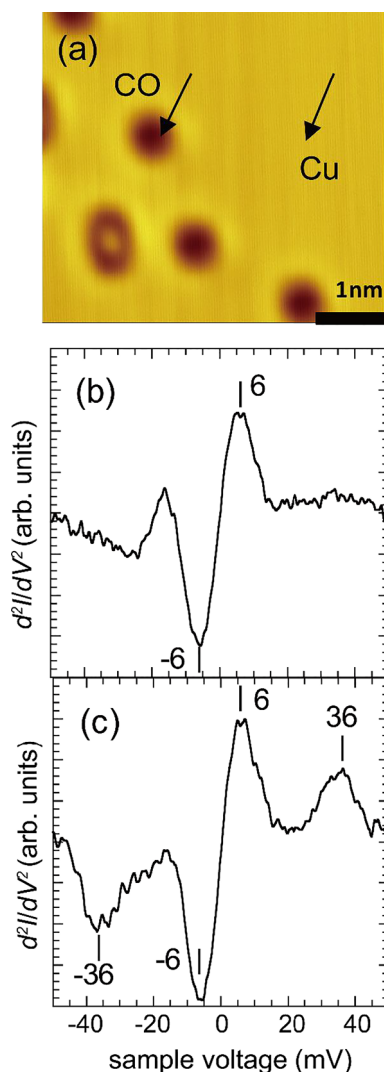
Fig. 2. (a) Topographic STM image of Cu(1 1 0) taken at 2 K in constant current mode with a sample voltage of −0.1 V and tunneling current of 0.2nA. The image size is 4.7 × 4.3 nm. The round depressions (dark contrast) are adsorbed CO molecules. IETS spectrum taken at (b) the clean area of Cu(1 1 0) and (c) the CO molecule. The black arrows in (a) indicate the tip positions where the IETS spectra (b) and (c) were taken. The spectra were recorded with a lock-in technique where a modulation voltage of Vrms = 8 mV at 315 Hz was added to the sample voltage. The vertical position of the tip was fixed at the sample voltage of −0.1 V and tunneling current of 0.2nA for each spectrum. Vertical bars highlight the positions of dips and peaks induced by the inelastic excitations. Adapted from Ref. [34].

slightly higher than reported values (3.1–5.0 meV) [40–42] and coincides with an energy of phonon mode in the clean surface, this low energy peak-dip pair might be originated from the combination of the FT mode and the phonon on the Cu(1 1 0) surface. The positions of peak-dip pairs originating from the vibrations on the clean and CO-adsorbed Cu(1 1 0) surfaces do not depend on the tip apex condition, which rules out the possibility that they originate from the vibrations relevant to the tip atoms. This means that the peak-dip pair observed for the clean area is intrinsic to the Cu(1 1 0) surface.

The phonon DOS of Cu(1 1 0) cannot explain the IETS spectrum for Cu(1 1 0). The peaks in the phonon DOS (see Fig. 3(a)) are mainly located at 20 and 25 meV, which are assigned to the MS_7 and S_7 modes, respectively [43,44]. Fig. 3(b) is the phonon DOS projected on the displacement of the topmost Cu layer atom along the (0 0 1), (1 $\bar{1}$ 0), and (1 1 0) direction. The S_1 surface phonon appears as a peak structure in projected phonon DOS around 8 meV. Even limited on the topmost layer, the entire phonon DOS spectrum does not match to the STM-IETS spectrum. Absence of a distinctive peak structure below 8 meV in the phonon DOS reflects the continuous phonon dispersions shown in Fig. 3(c). The single peak-dip pair at ± 6 mV is explained by the spectral shape of the momentum-resolved Eliashberg function as discussed herein.

We evaluate $M_{\Gamma\Gamma}^{\eta'\eta\lambda}$ by the *ab-initio* calculation based on the density functional perturbation theory (DFPT) [45]. Within the DFPT scheme, $M_{\Gamma\Gamma}^{\eta'\eta\lambda}$ is defined as

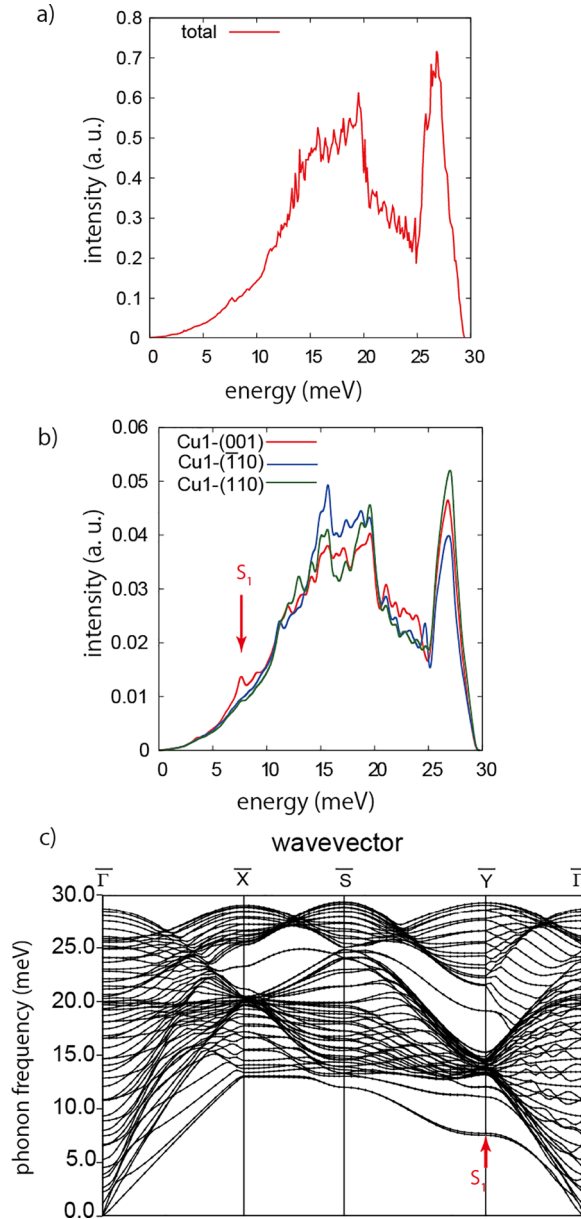**Fig. 3.** (a) The total phonon DOS. (b) The phonon DOS projected on the displacement of the topmost Cu layer atom along the (0 0 1), (1 1̄ 0), and (1 1 0) direction. (c) phonon dispersions calculated for the clean Cu(1 1 0) surface. All the ab-initio calculations were performed at the level of the generalized gradient approximation (GGA) with the Perdew-Burke-Ernzerhof (PBE) functional [84] by using QUANTUM-ESPRESSO [85]. The phonon DOS was obtained by the tetrahedron method [86] on a 21 × 21 × 1 uniform grid. The red arrow in phonon dispersion at the Ȳ point indicates the S1 surface phonon mode. The blue arrow at the Γ̄ point indicates the position of the mode that gives rise to the peak in Fig. 3(a). Adapted from Ref. [34].

$$M_{\bar{\Gamma}\bar{\Gamma}}^{\eta\eta'\lambda} = \sqrt{\frac{\hbar}{2M\omega_{\bar{\Gamma}}^{\lambda}}} < \bar{\Gamma}, \eta' | \frac{\delta V_{scf}(r)}{\delta R_{\bar{\Gamma}}^{\lambda}} | \bar{\Gamma}, \eta >,$$

(11)

with M being the mass of the atom. $|\bar{\Gamma}, \eta>$ is the Kohn-Sham state of the conduction electron with the band index η at the $\bar{\Gamma}$ point. $V_{scf}(r)$ is the self-consistent Kohn-Sham potential and $\frac{\delta V_{scf}(r)}{\delta R_{\bar{\Gamma}}^{\lambda}}$ corresponds to the first-order correction to the potential due to the atomic displacement R_q^{λ} attributed to the phonon mode λ at the $\bar{\Gamma}$ point with energy $\omega_{\bar{\Gamma}}^{\lambda}$. Note that $M_{\bar{\Gamma}\bar{\Gamma}}^{\eta'\eta\lambda}$ for acoustic phonons becomes zero at the $\bar{\Gamma}$ point, where their energy disperses to zero.

Fig. 4(a) shows the calculated $\alpha^2 F(\omega, k = q = 0)$ on the Cu(1 1 0) surface, which corresponds to the positive-bias side of the IETS spectrum. Whereas the phonon DOS limited to $q = 0$ exhibits several peaks in the low energy region in between 0 and 8 meV,
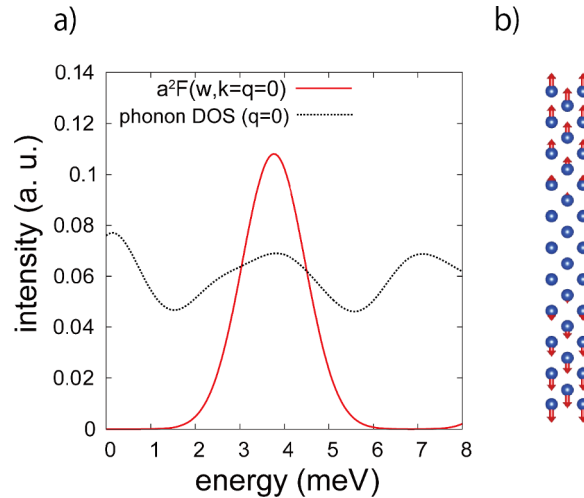
Fig. 4. (a) Calculated momentum-resolved Eliashberg function $\alpha^2 F(\omega, k = q = 0)$ (red line) and phonon DOS at the $\bar{\Gamma}$ point (black dotted line). $\delta(E_F - \varepsilon_i^{\eta'})$ and $\delta(eV - \omega_i^{\lambda})$ in the momentum-resolved Eliashberg function are approximated by the Gaussian functions with HWHM of $\sqrt{2\ln 2} \times 50$ and $\sqrt{2\ln 2}$ meV, respectively. In the calculation, the summation is carried out on whole indices of phonon mode and conduction band at the $\bar{\Gamma}$ point (λ, η, η'). The phonon density of states at the $\bar{\Gamma}$ point is obtained by the smearing of the discrete phonon eigenvalue spectrum at the $\bar{\Gamma}$ point by the Gaussian function with a HWHM of $\sqrt{2\ln 2}$ meV. (b) Displacement pattern of respective Cu atoms for the phonon mode which gives rise to the peak at 4 meV in the momentum-resolved Eliashberg function. The blue spheres correspond to the Cu atoms in the slab model. The lengths of the red arrows correspond to the amplitude of the displacement. This figure is rendered by VESTA [87]. Adapted from Ref. [34]. (For interpretation of the references to color in this figure legend, the reader is referred to the web version of this article.)

$\alpha^2 F(\omega, k = q = 0)$ shows the salient single peak around 4 meV. This spectral shape with single peak coincides with the IETS spectrum shown in Fig. 2.

These results show that the STM-IETS spectrum is determined by EPC. The phonon mode observed by STM-IETS is different from those by the other vibrational spectroscopies [43,46–49]. The peak at 6 meV in STM-IETS spectrum on Cu(1 1 0) is assigned to the out-of-plane polarized phonon mode whose atomic displacements mainly distribute in the several top layers of the Cu(1 1 0) surface as shown in Fig. 4(b). This mode has never observed by HAS [46,47], HREELS [43,48] and inelastic Laser Photoemission Spectroscopy (ILPES) [49]. In the HAS study of Manson et al. [46], multiple dispersions derived from acoustic phonons are observed extending from 0 to about 10 meV. These results are confirmed by the HAS study of Zeppenfeld et al. [47], who observe the other phonon dispersions including MS_7 surface phonon resonance around 20 meV. The HREELS studies show that the MS_7 phonon appears at about 20 meV for the $\bar{\Gamma}$ point [43,48]. In the ILPES study [49], a replica of the Fermi edge is observed at 14.7 meV below E_F in the normal emission configuration, which is originated from the excitation of surface phonon by a photoexcited electron. All these previous studies do not show that the surface phonon mode is observed around 4–6 meV. This is rationalized by considering the excitation mechanism. The excitation of surface phonon occurs through the deformation of He atom-surface potential induced by surface phonon in HAS so that HAS does not probe EPC directly. In the HREELS studies, the MS_7 phonon is mainly excited by the dipole scattering in which an incident electron excites the phonon through coupling with the dipole field caused by the phonon [3]. The excitation mechanism in ILPES is relatively similar to that in STM-IETS [49]. In ILPES, a phonon mode of larger EPC is selectively excited when the photoexcited electron passes through the surface in ILPES. The main difference between ILPES and STM-IETS is the energy of electron. In the latter, tunneling electron passes through electronic states around E_F while the photoexcited electron passes above the vacuum level in the former. Since EPC depends on the energy and momentum of electron as discussed above, the different phonon modes are excited and consequently distinctive spectral features are observed.

The main conclusion here is that the STM-IETS spectrum proportional to the momentum resolved Eliashberg function. Recently, Jandke et al. also reported the application of similar formalism to the superconducting state, and revealed the fingerprint of the phonon responsible for the Cooper pairing [50]. Future theoretical and experimental studies of systems with strong EPC with atomic resolution present interesting topics.

3. STM-IETS for solid interfaces

In this section, we introduce the application of STM-IETS for detecting interfacial phonons. The previous section introduced the theoretical formula of STM-IETS for a uniform solid surface and demonstrated that STM-IETS observes the momentum-resolved Eliashberg function in the substrate. If the substrate side has an interface along the vertical direction, the tunneling electron can also excite the interfacial phonons. In this case, we must address the possible spatial dependence of the IETS spectrum arising from the electronic and phononic structures and EPC modulated by the complex interfacial structure. Because the theoretical formalism discussed in the previous section is constructed in momentum space, it is not suitable to describe the variation of IETS spectrum in real space. Thus, we must choose a different strategy to connect the STM-IETS signal derived from the interface with a realistic atomic
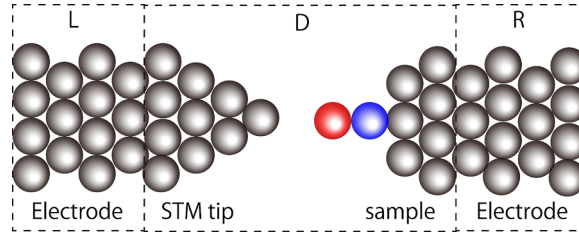
Fig. 5. Schematic image of two-terminal setup model in STM simulation by atomistic NEGF + DFT method.

structure. The most suitable framework to meet these criteria is the combination of the NEGF transport theory and DFT calculations using atomic-like basis sets, which has been applied to various nanojunctions including molecular adsorption systems [31,51]. Hereafter we call this framework atomistic NEGF + DFT.

The following discussion introduces the theoretical background of the atomistic NEGF + DFT method for STM-IETS simulation and its application to the interfacial phonons of epitaxial graphene grown on SiC(0 0 0 1).

3.1. 3.1 Atomistic NEGF + DFT approach for STM-IETS simulations

In the STM-IETS simulation with the atomistic NEGF + DFT method, the experimental setup is modeled by the extension of the two-terminal setup of Meir-Wingreen formulation [52] as schematically shown in Fig. 5. The model consists of the left lead (L), device region (D), and right lead (R). The Green's functions in each region are evaluated from DFT calculations by the atomic-like basis set as described herein [31].

Using the basis orbitals $\{|i\rangle\}$ that are localized at respective atoms in the model, the eigenstates of the effective single-particle Hamiltonian $\mathbf{H}$ can be expanded as

$$\Psi_\mu = \sum_i c_{i\mu} |i\rangle. \tag{12}$$

The coefficient $c_{i\mu}$ is determined by solving the generalized eigenvalue problem

$$\sum_j (H_{ij} - E_\mu S_{ij}) c_{j\mu} = 0 \tag{13}$$

where $H_{ij} = \langle i|H|j \rangle$ and $S_{ij} = \langle i|j \rangle$ represent finite overlap matrix elements. The two matrices $\mathbf{H} = \{\{H_{ij}\}\}$ and $\mathbf{S} = \{\{S_{ij}\}\}$ are divided into block matrices corresponding to the three regions (L, D and R) and interaction between them as follows:

$$\mathbf{H} = \begin{pmatrix} \mathbf{H}_L & \mathbf{H}_{LD} & 0 \\ \mathbf{H}_{DL} & \mathbf{H}_D & \mathbf{H}_{DR} \\ 0 & \mathbf{H}_{RD} & \mathbf{H}_R \end{pmatrix}, \tag{14}$$

$$\mathbf{S} = \begin{pmatrix} \mathbf{S}_L & \mathbf{S}_{LD} & 0 \\ \mathbf{S}_{DL} & \mathbf{S}_D & \mathbf{S}_{DR} \\ 0 & \mathbf{S}_{RD} & \mathbf{S}_R \end{pmatrix}. \tag{15}$$

In the appropriate model setup where the L and R regions are well separated, the coupling and overlap between them becomes negligible. Therefore, we set $\mathbf{H}_{LR} = \mathbf{H}_{RL} = \mathbf{S}_{LR} = \mathbf{S}_{RL} = 0$ in Eqs. (14) and (15). By using these block matrices, the non-perturbed (without EPC) retarded Green's function in the device region $\mathbf{G}_D^{0,r}(\varepsilon)$ can be expressed as

$$\mathbf{G}_D^{0,r}(\varepsilon) = [(\varepsilon + i\delta)\mathbf{S}_D - \mathbf{H}_D - \Sigma_L^r(\varepsilon) - \Sigma_R^r(\varepsilon)]^{-1} \tag{16}$$

$$\Sigma_L^r(\varepsilon) = (\mathbf{H}_{DL} - \varepsilon\mathbf{S}_{DL})\mathbf{g}_L^r(\varepsilon)(\mathbf{H}_{LD} - \varepsilon\mathbf{S}_{LD}) \tag{17}$$

$$\Sigma_R^r(\varepsilon) = (\mathbf{H}_{DR} - \varepsilon\mathbf{S}_{DR})\mathbf{g}_R^r(\varepsilon)(\mathbf{H}_{RD} - \varepsilon\mathbf{S}_{RD}) \tag{18}$$

where $\mathbf{g}_L^r(\varepsilon)$ and $\mathbf{g}_R^r(\varepsilon)$ are the retarded Green's functions for the semi-infinite left and right leads, respectively. In the computational process, at first, the structural model is constructed from the device region sandwiched by the left and right leads with finite size. The elements of $\mathbf{H}$ and $\mathbf{S}$ are obtained for this structural model. Then, $\mathbf{g}_L^r(\varepsilon)$ and $\mathbf{g}_R^r(\varepsilon)$ for semi-infinite leads are calculated by the recursive techniques using the bulk states of the respective leads obtained from separate calculations. In combination with SIESTA [53] and TRANSIESTA [51,54], these Green's functions and the self-energies $\Sigma_{R,L}^r(\varepsilon)$ are directly obtained in DFT calculations.

The steady-state electric current flows from a metallic lead to the device region D as defined in the following:

$$I_\alpha = 2e\frac{dN_\alpha}{dt} = \frac{-2e}{\hbar} \int_{-\infty}^{\infty} \frac{d\varepsilon}{2\pi} \text{Tr}\,[\Sigma_\alpha^<(\varepsilon)\mathbf{G}_D^>(\varepsilon) - \Sigma_\alpha^>(\varepsilon)\mathbf{G}_D^<(\varepsilon)], \tag{19}$$

where N_α is the number of electrons in the lead $\alpha = $ L or R and $\mathbf{G}_D^>(\varepsilon)$ ($\mathbf{G}_D^<(\varepsilon)$) is the full lesser (greater) Green's function including EPC in the device region D. $\Sigma_\alpha^>(\varepsilon)$ ($\Sigma_\alpha^<(\varepsilon)$) is the lesser (greater) self-energy introduced by the interaction between the lead and device

region. The lesser (greater) self-energy represents the rate of electron scattering into (out of) the device region and defined as

$$\Sigma_\alpha^<(\varepsilon) = -n_F(\varepsilon - \mu_\alpha)[\Sigma_\alpha^r(\varepsilon) - \Sigma_\alpha^a(\varepsilon)], \tag{20}$$

$$\Sigma_\alpha^>(\varepsilon) = -[n_F(\varepsilon - \mu_\alpha) - 1][\Sigma_\alpha^r(\varepsilon) - \Sigma_\alpha^a(\varepsilon)]. \tag{21}$$

Here $n_F(\varepsilon)$ is the Fermi-Dirac distribution and μ_α is the chemical potential of the lead α.

The derivation of Eq. (19) is similar to those of Eqs. (2) and (3). The main difference is that the Green's functions and self-energies in Eq. (19) take the matrix representations with the atomic basis orbitals. The full lesser and greater Green's functions in Eq. (19) can be evaluated from the retarded and advanced ones through the Keldysh equations

$$\mathbf{G}_D^<(\varepsilon) = \mathbf{G}_D^r(\varepsilon)\{\Sigma_L^<(\varepsilon) + \Sigma_R^<(\varepsilon) + \Sigma_{ph}^<(\varepsilon)\}\mathbf{G}_D^a(\varepsilon), \tag{22}$$

$$\mathbf{G}_D^>(\varepsilon) = \mathbf{G}_D^r(\varepsilon)\{\Sigma_L^>(\varepsilon) + \Sigma_R^>(\varepsilon) + \Sigma_{ph}^>(\varepsilon)\}\mathbf{G}_D^a(\varepsilon). \tag{23}$$

The full retarded Green's function fulfills the Dyson equation

$$\mathbf{G}_D^r(\varepsilon) = \mathbf{G}_D^{0r}(\varepsilon) + \mathbf{G}_D^{0r}(\varepsilon)\Sigma_{ph}^r(\varepsilon)\mathbf{G}_D^r(\varepsilon). \tag{24}$$

Therefore, we also must calculate the phonon self-energies, $\Sigma_{ph}^{\gtrless}(\varepsilon)$ and $\Sigma_{ph}^r(\varepsilon)$. These energies are obtained from the normal mode resolved self-energies $\Sigma_{ph,\lambda}^>(\varepsilon)$, $\Sigma_{ph,\lambda}^<(\varepsilon)$ and $\Sigma_{ph,\lambda}^r(\varepsilon)$ using the following equations:

$$\Sigma_{ph,\lambda}^>(\varepsilon) = i \int_{-\infty}^{\infty} \frac{d\varepsilon'}{2\pi} \mathbf{M}^\lambda d_0^>(\lambda, \varepsilon - \varepsilon') \mathbf{G}_D^>(\varepsilon) \mathbf{M}^\lambda, \tag{25}$$

$$\Sigma_{ph,\lambda}^<(\varepsilon) = i \int_{-\infty}^{\infty} \frac{d\varepsilon'}{2\pi} \mathbf{M}^\lambda d_0^<(\lambda, \varepsilon - \varepsilon') \mathbf{G}_D^<(\varepsilon') \mathbf{M}^\lambda, \tag{26}$$

$$\Sigma_{ph,\lambda}^r(\varepsilon') = \frac{1}{2}[\Sigma_{ph,\lambda}^>(\varepsilon) - \Sigma_{ph,\lambda}^<(\varepsilon)] - iP \int_{-\infty}^{\infty} \frac{d\varepsilon'}{2\pi} \frac{[\Sigma_{ph,\lambda}^>(\varepsilon') - \Sigma_{ph,\lambda}^<(\varepsilon')]}{\varepsilon' - \varepsilon}. \tag{27}$$

Here, $d_0^>(\lambda, \omega)$ ($d_0^<(\lambda, \omega)$) is the lesser (greater) free phonon Green's function which is defined as

$$d_0^>(\lambda, \omega) = -2\pi i[\langle n_\lambda \rangle \delta(\omega - \omega_\lambda) + (\langle n_\lambda \rangle + 1)\delta(\omega + \omega_\lambda)], \tag{28}$$

$$d_0^<(\lambda, \omega) = -2\pi i[\langle n_\lambda \rangle \delta(\omega + \omega_\lambda) + (\langle n_\lambda \rangle + 1)\delta(\omega - \omega_\lambda)]. \tag{29}$$

where n_λ is the phonon occupation number of mode λ. $\mathbf{M}^\lambda$ is the EPC matrix which can be evaluated from the derivative of the Hamiltonian matrices and orbital overlaps with respect to the atomic displacement caused by phonons [31]. Once we determine $\Sigma_\alpha^r(\varepsilon)$, $\Sigma_\alpha^a(\varepsilon)$, $\mathbf{M}^\lambda$, and ω_λ from the DFT calculations, the tunneling current and its derivatives are calculated from Eq. (19). The self-consistent Born approximations of these equations are demanding and the lowest-order expansion is often adopted in which $\mathbf{G}_D^{r/a}(\varepsilon)$ in Eqs. (22)–(24) are replaced by non-perturbed ones $\mathbf{G}_D^{0r/a}(\varepsilon)$. The set of Eqs. (19)–(29) are computed with the combination of the INELASTICA [31] and SIESTA/TRANSIESTA packages.

3.2. STM-IETS for epitaxial graphene on SiC(0 0 0 1)

Here we introduce our investigation on epitaxial graphene grown on SiC(0 0 0 1) [35]. To the best of our knowledge, our work reflects the first example of STM-IETS for interfacial phonons. On the Si-terminated 4H-SiC(0 0 0 1) surface, graphene is epitaxially grown by the thermal decomposition of SiC. This method provides wafer-scale and high-quality graphene sheets on the insulating substrate. The fabricated graphene is a promising system to realize graphene-based nanodevices [55–59]. The insulating SiC substrate changes the physical properties of graphene through the interfacial phonon from the free-standing state. One of the most bothersome effects is the serious reduction of the electron mobility, which is caused by the electron-phonon scattering at the interface [60–63]. It
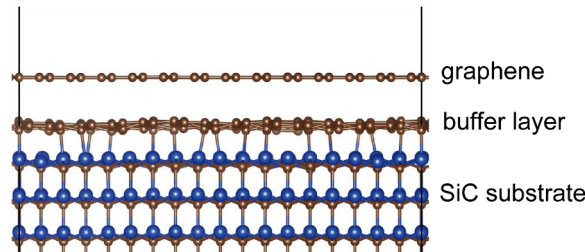

Fig. 6. Cross-sectional view of the structure model of epitaxial graphene grown on 4H-SiC(0 0 0 1) surface. The plane where the cross-sectional view is taken corresponds to the black line denoted as cut 1 in Fig. 7(b). A carbon layer exhibits beneath the graphene layer working as a buffer layer to separate the graphene layer from the SiC substrate. This buffer layer has a reconstruction with $6\sqrt{3} \times 6\sqrt{3}\,R30$ periodicity whose one cycle period is indicated by black solid line. Adapted from Ref. [35].
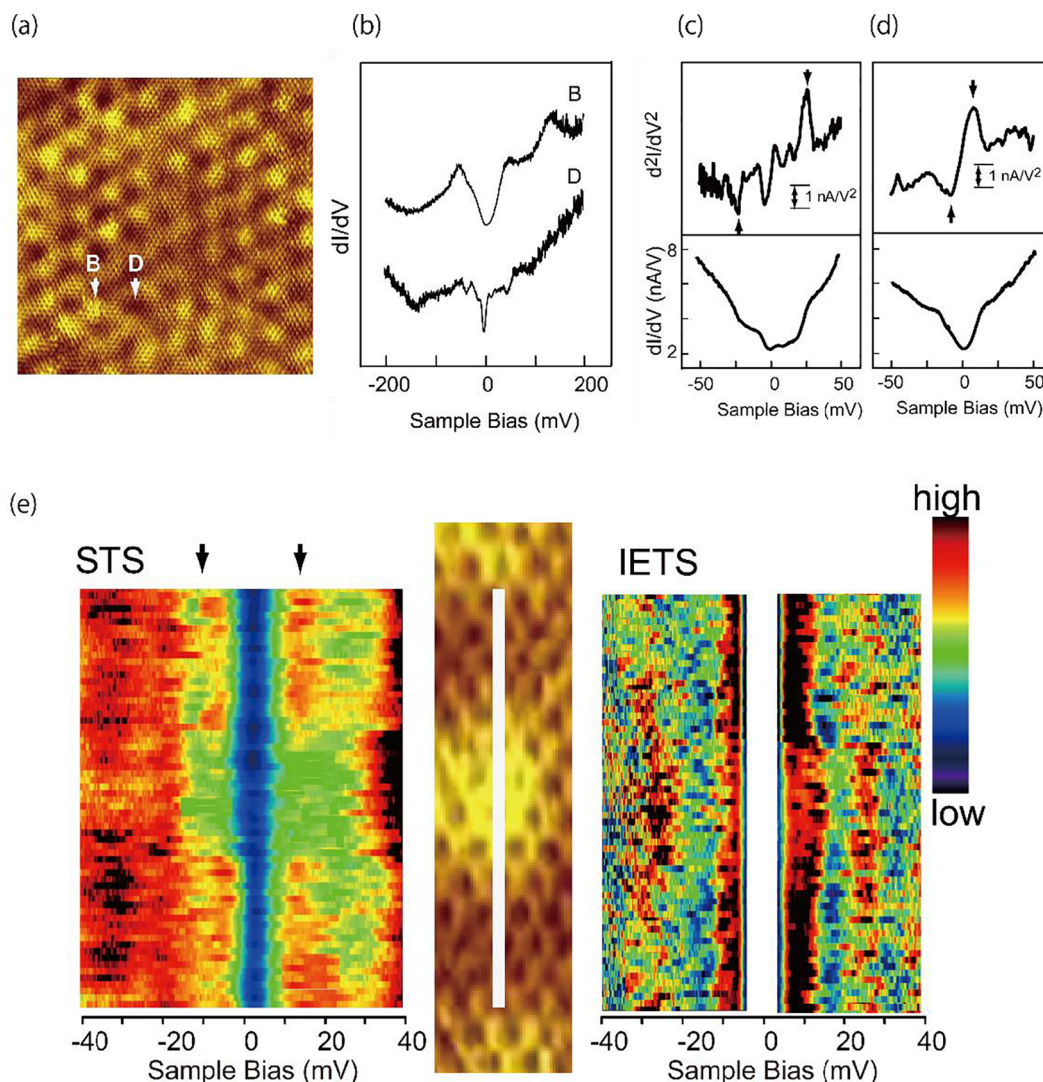
Fig. 7. (a) STM topographic image of epitaxial graphene grown on a SiC(0 0 0 1) surface. Area $14 \times 14\,\text{nm}^2$, and set point of I = 0.8nA and V = −200 mV. Brighter color represents the charge accumulation. (b) STS spectra obtained at the bright (B) and dark (D) areas of the topographic image. (c, d) dI/dV and d^2I/dV^2 spectra obtained at B and D areas. Black arrows in (c) and (d) indicate the energy at which the prominent inelastic phonon excitation occurs. (e) Spatial distribution of dI/dV (left panel) and d^2I/dV^2 (right panel). The series of dI/dV and d^2I/dV^2 are taken along the white line that connects the neighboring bright spots in the STM topographic image shown in the center panel. The horizontal axis corresponds to the sample bias and the vertical axis corresponds to the measured position (corresponding directly to the right panel) and the intensity of the d^2I/dV^2 spectrum is expressed according to a color table. For d^2I/dV^2, the contrast is reversed in the positive and negative energy regions for a clear view. Adapted from Ref. [35].

is therefore important to reveal and understand the precise nature of the responsible interfacial phonon.

The graphene/SiC interface possesses a characteristic atomic structure. As shown in Fig. 6, there is a carbon layer beneath the graphene layer. This carbon buffer layer reconstructs into a $6\sqrt{3} \times 6\sqrt{3}R30$ superstructure with respect to the unit cell of the SiC surface [58,64–66]. We hereafter denote this structure as $6\sqrt{3}$. The superstructure results in several types of interfacial Si and C atoms in different local environments. Previous *ab-initio* calculations showed that the interfacial electronic states are strongly affected by the local atomic environment and have a spatial variation [67–69]. These results suggest that the phonon properties at the interface should also have spatial dependence.

Our STM/STS and STM-IETS measurements certainly show that the spatial dependence of the phonon excitation signal correlates with the superstructure. Fig. 7(a) is a typical topographic image of the epitaxial graphene grown on the SiC(0 0 0 1) surface. The image shows a long-range superstructure with the $6\sqrt{3}$ periodicity induced by the interfacial reconstruction in addition to the atomic protrusions. These characteristics are consistent with the results of previous work [70–72]. The bright and dark areas specified by arrows are labeled B and D, respectively. The dI/dV spectra measured at the B and D areas are shown in Fig. 7(b). Both dI/dV spectra exhibit a gap near the Fermi level. This gap shows a marked dependence on the lateral tip position; the gap measured at the B area is
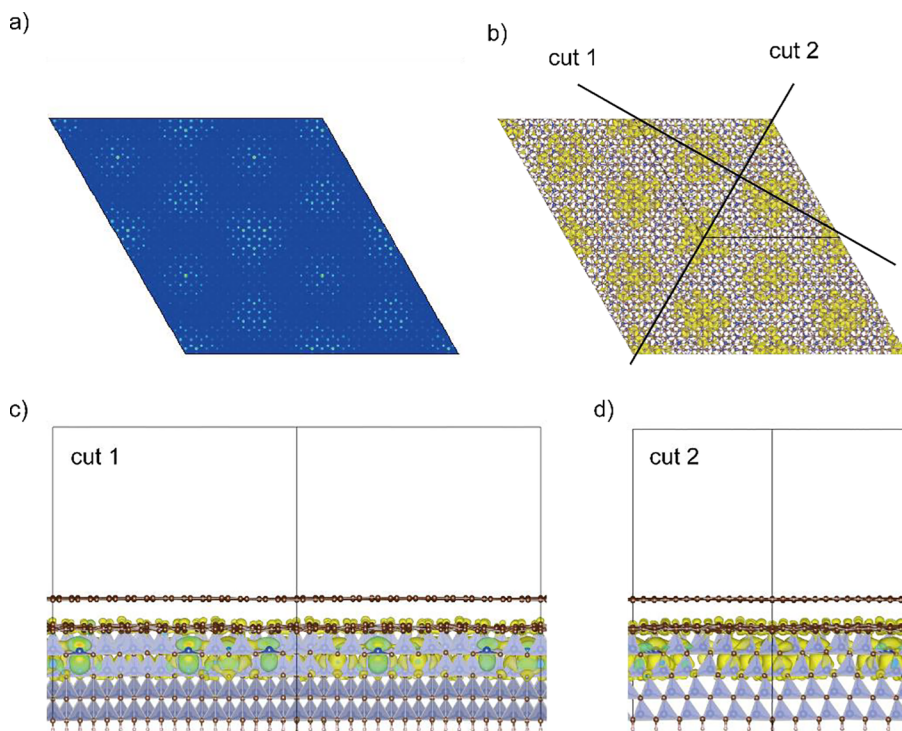
Fig. 8. (a) STM simulation results at −100 mV sample bias voltage. STM simulation is carried out using the Vienna Ab-initio Simulation Package (VASP) [88,89] with projected augmented wave (PAW) pseudo potential [90]. The local-density approximation exchange correlation functional was used. (b) Partial charge distribution used for plotting (a). The black lines indicate the planes where the cross-sectional views shown in (c) and (d) are taken. (c and d) Cross-sectional images of the partial charge distribution taken on the cut 1 and cut 2 plane in (b), respectively. The blue-gray surfaces are the tetrahedron of C centered by a Si atom. The charge distribution becomes dense at the Si atom with dangling bond that is not surrounded by the tetrahedral plane. Adapted from Ref. [35]. (For interpretation of the references to color in this figure legend, the reader is referred to the web version of this article.)

wider than that at the D area.

The gap structure is attributed to the excitations of the interfacial phonons via the inelastic tunneling process because the energy and its spatial variation are not well explained by the intrinsic electronic structure of graphene. The dI/dV spectrum obtained at B shows a staircase increase, which corresponds to the peak at $+24$ meV and the dip at $−24$ meV in the d^2I/dV^2 spectrum (see arrows in Fig. 7(c)). On the other hand, the d^2I/dV^2 spectrum obtained at D shows a peak-and-dip pair at ± 9 meV as shown by the arrows in Fig. 7(d). Comparing the STM image and the spatial variations in the dI/dV and the d^2I/dV^2 spectra reveals a clear correlation between them, as shown in Fig. 7(e).

In order to elucidate the mechanism of possible phonon excitation and the origin of the spatial modulation of the IETS spectrum, we carried out a theoretical analysis. First, we simulated the STM image using DFT calculations and revealed the correlation of the topographic image with the interfacial atomic/electronic structures. Fig. 8(a) shows the simulated STM image for the $6\sqrt{3}$ structure with a bias voltage of $−100$ mV, and Fig. 8(b)–(d) show the top-view and cross-sectional distributions of the partial charge density in the energy range between $−100$ and 0 meV. Comparing these images, we found that the region with the highest charge density, i.e., the brightest region in the simulated image, stems from the dangling bond of the Si atom at the interface. In contrast, the interfacial Si atoms placed beneath the C atoms in the buffer layer appear darker in the topographic image. This is because each dangling bond is terminated by the bonding with the C atom so that the partial charge density significantly decreases at the Si atom. Therefore, we conclude that the dangling bond of the interfacial Si atom determines the contrast of the STM topographic image.

We inferred from the correlation between the periodicity in the STM topographic image and the IETS signal that the presence or absence of a Si dangling bond gives rise to the spatial variation of the IETS signal. In order to confirm this inference, we carried out *ab-initio* calculations of the phonon properties and the dI/dV spectra including inelastic tunneling. In these calculations, we used the smaller structural model of a $\sqrt{3} \times \sqrt{3}R30$ periodicity (Fig. 9(a)) instead of the $6\sqrt{3}$ structure in order to reduce the computational cost. This $\sqrt{3} \times \sqrt{3}R30$ model, hereafter denoted by $\sqrt{3}$, contains essentially the same local environments as those in the $6\sqrt{3}$ structure; the relative geometric configurations are held among the C atoms in the topmost graphene layer, the C atoms in the buffer layer and the interfacial Si atoms. The C atoms in the graphene can be classified into four types as indicated by the different colors in the right panel of Fig. 9(a). The C atoms in the buffer layer are also classified as with or without the C–Si bonding, and the Si atoms are distinguished as with or without the dangling bond. This $\sqrt{3}$ model was used in previous studies and well reproduces the ARPES experimental results [69] and the Raman spectra from the buffer layer [73].
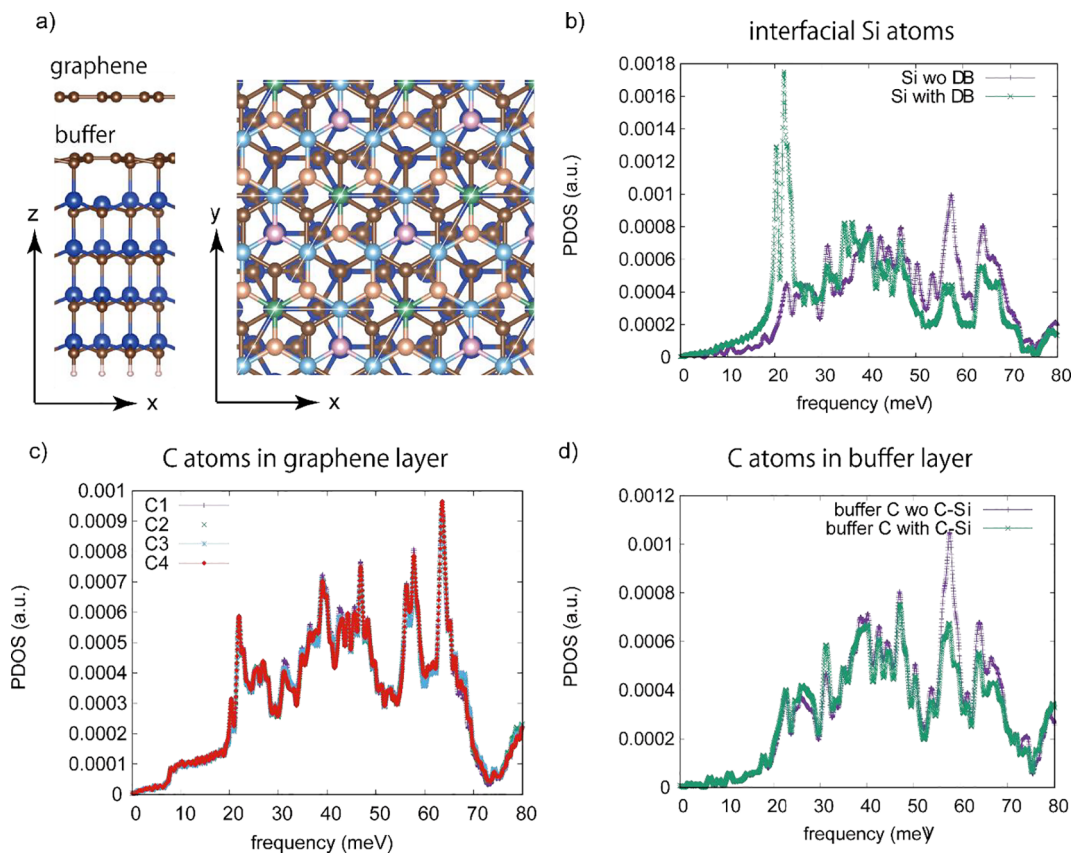
a)

graphene

buffer

b) interfacial Si atoms

c) C atoms in graphene layer

d) C atoms in buffer layer

Fig. 9. (a) Geometric structure of the $\sqrt{3}$ model of epitaxial graphene on 4H-SiC (0 0 0 1). (Left) Side and (Right) top views of the structural model; brown, C; blue, Si; light pink, H atoms. The four different colors of the C atoms in the topmost graphene layer correspond to the different chemical environments; light green, C1 type atoms positioned on the top of the buffer C and interfacial Si atom; light blue, C2 type atoms also positioned on top of the buffer C atom, but with no interfacial Si atom beneath; orange, C3 type atoms where there is no buffer C atom or interfacial Si atom beneath; pink, C4 type atoms positioned on the top of the interfacial Si atom with dangling bond. (b–d) Phonon DOS of the z-polarized mode projected on the interfacial Si atoms, the C atoms in the graphene layer, and the C atoms in the buffer layer, respectively. These phonon properties in the $\sqrt{3}$ model are calculated by using density functional perturbation theory (DFPT) [45] implemented in the Quantum-Espresso (QE) package [85] with local-density approximation exchange correlation functional. Adapted from Ref. [35]. (For interpretation of the references to color in this figure legend, the reader is referred to the web version of this article.)

The phonon DOS projected on the respective types of C and Si atoms are shown in Fig. 9(b)–(d). In the low-energy region below 50 meV, the z-polarized phonon modes are dominant, and we focus on these modes in the analysis of phonon DOS. The projected phonon DOS of z-polarized modes obtained at the interfacial Si atoms indeed shows a clear spatial dependence (Fig. 9(b)). The pronounced peak structure near 24 meV appears at the Si atoms with the dangling bond, whereas the peak disappears at the Si atoms without the dangling bond. In contrast, the phonon DOS projected on the C atoms in the graphene layer shows a negligible difference among four types of C atoms (Fig. 9(c)). For the C atom in the buffer layer, the phonon DOS depends on the presence of the C-Si covalent bond (Fig. 9(d)). The difference mainly appears in the higher energy range (> 80 meV), and the relevant phonons can be ruled out from the origin of the spatial variation of the STM-IETS spectrum observed below 50 meV.

The calculated phonon DOS indicates that the spatial dependence of the low-energy phonon excitations is attributed to the presence or absence of the dangling bond of the interfacial Si atoms. However, the phonon DOS alone cannot explain the STM-IETS spectral shape. Although there are many peaks in the phonon DOS as shown in Fig. 9(b)–(d), most of them do not appear in the IETS spectrum. In order to fully understand the mechanism of the phonon excitation and mode selectivity, we must account for the actual electron transport process and the effect of EPC in the graphene-SiC interface. Such simulation becomes possible by the theory introduced in Section 3.1, which is implemented in INELASTICA [31].

In the simulations by INELASTICA, we selected two representative model structures for the dark (D) and bright (B) regions as shown in Fig. 10(a). In both models, the STM tip is represented by a chain of gold atoms. In the D (B) model, we set the tip above the graphene C atom positioned on top of the Si atom without (with) the dangling bond. The definition of the device region and the unit cell for two electrodes is also shown in Fig. 10(a).

The calculated dI/dV spectra agree closely with the experimental findings (Fig. 10(b)). First, the intensity of the dI/dV spectrum at the same tip-sample distance is much larger in the B model than that in the D model, which reproduces the contrast in the STM
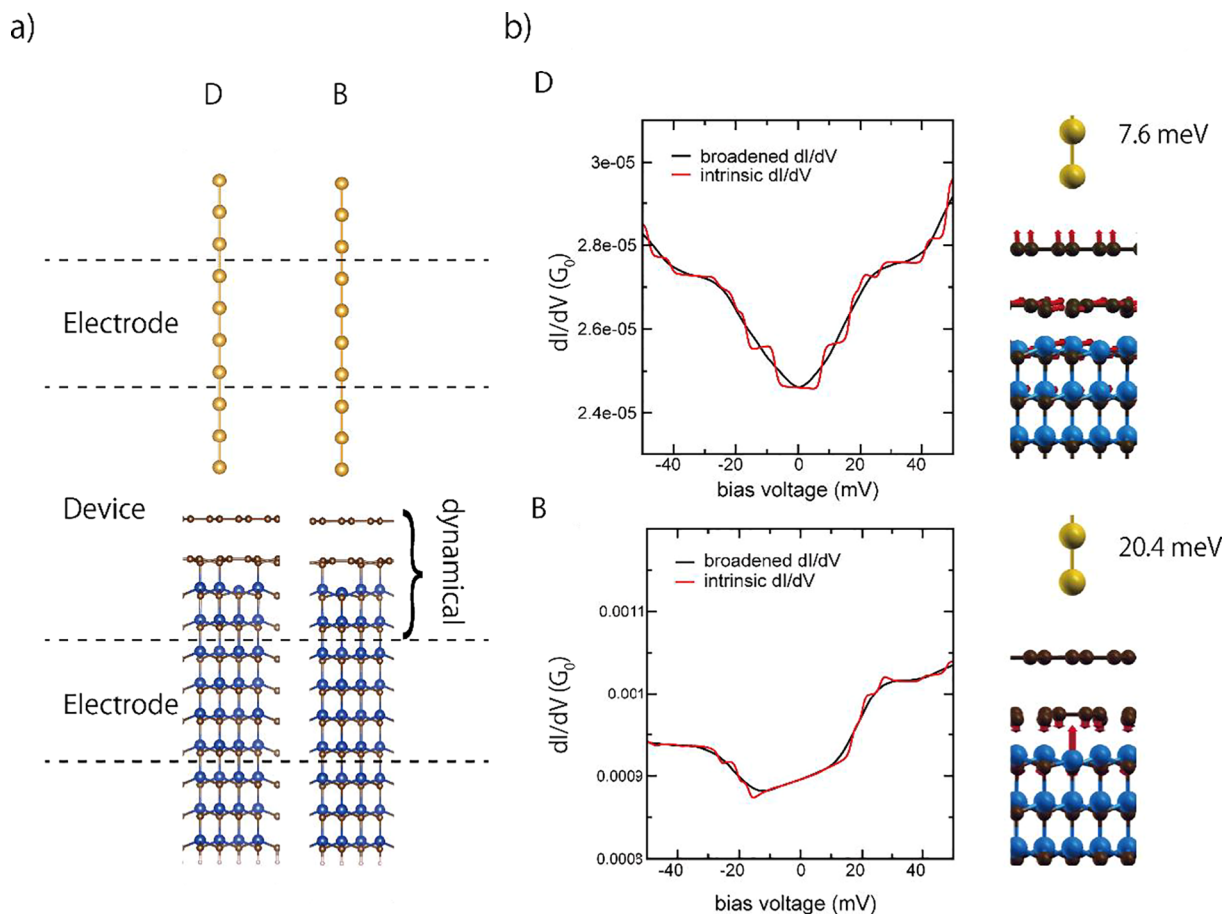
Fig. 10. (a) Two structural models (D and B) used in the *dI/dV* calculations with INELASTICA. (b) Simulated *dI/dV* in the D and B models. Black lines show the calculated *dI/dV* spectra which are broadened numerically by taking the modulation voltage used in the lock-in measurement technique (Vrms = 5 mV). Red lines are the intrinsic dI/dV results (linewidth only due to a finite temperature of T = 4.2 K). The structural side views show the displacements of the atoms in the active phonon modes that contribute to the narrow (7.6 meV) and wide (20.4 meV) gaps, respectively. Adapted from Ref. [35]. (For interpretation of the references to color in this figure legend, the reader is referred to the web version of this article.)

topographic image. Second, the gap widths in the *dI/dV* spectra calculated for both B and D models match those measured in the B and D areas. In the B model, the gap is ~40 meV, which is much wider than that in the D model (~20 meV). The wider gap structure originates from the phonon mode of 20.4 meV, which corresponds to the z-polarized motion of the interfacial Si atom with the dangling bond. This phonon mode appears as a sharp peak structure in the phonon DOS shown in Fig. 10(b). In addition to this mode, the low-frequency phonon mode of 7.6 meV is excited in the D model, which rationalizes the smaller gap. This low-frequency mode is the combination of the out-of-plane vibration of the outermost graphene layer and in-plane vibration of the buffer layer.

We would like to note that the interfacial phonon with ~20 meV reported here is different from the interfacial phonons studied in previous investigations, e.g., the optical phonon mode of the SiC surface [74,75], the interlayer longitudinal optical mode [75], vibration of interfacial defects [76], and the acoustic mode of the buffer layer [62]. This phonon mode would be active at room temperature because of its low energy and would become a source of remote interfacial phonon scattering [74] which degrades the carrier mobility.

4. Summary

In this review article, we introduced our combined studies of STM-IETS experiments and theoretical approaches using nonequilibrium Green's functions and DFT calculations. We presented two examples. In the first one, the theoretical formalism was constructed in the electron and phonon momentum spaces to elucidate the basic mechanism of phonon excitations by tunneling electrons. This theory demonstrates that the low-energy phonon emerging in the STM-IETS spectrum is rationalized by the momentum-resolved Eliashberg function on metal surfaces. The theory is successfully applied to the surface phonon excitation on Cu (1 1 0). In the second example, the application of the atomistic NEGF + DFT method implemented in INELASTICA to the interfacial phonons at the graphene-SiC interface was presented. The spatial variations of STM-IETS spectra measured for the complex interface

are nicely reproduced. This example demonstrates that the combination of experimental and computational STM-IETS enables us to investigate buried interfaces by measuring and analyzing the interfacial phonons.

Both examples reveal that it is central to evaluate the EPC quantitatively for understanding the phonon excitations in STM-IETS. Until recently, it was challenging to evaluate the EPC constants and Eliashberg functions of realistic materials so that these physical quantities were treated as fitting parameters to rationalize the experimental results. The recent progress in the theoretical approaches enables us to calculate the EPC constants and the Eliashberg functions in the DFT level for realistic materials. More recently, the combination of maximally localized Wannier function (MLWF) [77] and DFPT methods helps us calculate the EPC constants on the finer meshes of electron and phonon wavenumbers [78]. Indeed, such a DFPT + MLWF method has been successfully applied to calculate the Eliashberg functions of various superconducting materials [79–83]. Combining the theoretical methods introduced in this review and these computational approaches, the phonon spectroscopies by STM-IETS would be a more powerful tool to explore the phonon-related physics in a wider range of materials such as superconductor, 2D materials, van der Waals heterostructures, also artificial lattices of semiconductors and transition metal oxides.

Acknowledgements

References

[1] G. Grosso, G.P. Parravinici, Solid State Physics, Academic Press, New York, 2000.
[2] G.D. Mahan, Many-Particle Physics, Kluwer Academic/Plenum Publishers, 1981.
[3] H. Ibach, D.L. Mills, Electron Energy Loss Spectroscopy and Surface Vibrations, Academic Press, New York, 1982.
[4] T. Kondo, Compendium of Surface and Interface Analysis, Springer Singapore, Singapore, 2018, p. 239.
[5] J.P. Toennies, J. Phys.: Condens. Matter 5 (1993) A25.
[6] J.T. Yates, T.E. Madey, Vibrational Spectroscopy of Molecules on Surfaces, Springer, US, New York, 1987.
[7] A.K. Geim, K.S. Novoselov, Nat. Mater. 6 (2007) 183.
[8] A. Acun, et al., J. Phys.: Condens. Matter 27 (2015) 443002.
[9] Y. Junji, F. Yuya, N. Kazuki, I. Naoki, N. Masashi, X. Lede, R. Angel, L. Guy Le, 2D Materials 5 (2018) 025002.
[10] N. Takagi, C.-L. Lin, K. Kawahara, E. Minamitani, N. Tsukahara, M. Kawai, R. Arafune, Prog. Surf. Sci. 90 (2015) 1.
[11] J. Zhao, et al., Prog. Mater. Sci. 83 (2016) 24.
[12] G.R. Bhimanapati, et al., ACS Nano 9 (2015) 11509.
[13] W. Choi, N. Choudhary, G.H. Han, J. Park, D. Akinwande, Y.H. Lee, Mater. Today 20 (2017) 116.
[14] B.C. Stipe, M.A. Rezaei, W. Ho, Science 280 (1998) 1732.
[15] W. Ho, J. Chem. Phys. 117 (2002) 11033.
[16] T. Komeda, Prog. Surf. Sci. 78 (2005) 41.
[17] J.I. Pascual, Eur. Phys. J. D: Atom. Mol. Opt. Plasma Phys. 35 (2005) 327.
[18] Y. Kim, T. Komeda, M. Kawai, Phys. Rev. Lett. 89 (2002) 126104.
[19] Y. Kim, K. Motobayashi, T. Frederiksen, H. Ueba, M. Kawai, Prog. Surf. Sci. 90 (2015) 85.
[20] T. Komeda, Y. Kim, M. Kawai, B.N.J. Persson, H. Ueba, Science 295 (2002) 2055.
[21] T. Kumagai, Prog. Surf. Sci. 90 (2015) 239.
[22] G. Binnig, N. Garcia, H. Rohrer, Phys. Rev. B 32 (1985) 1336.
[23] B.N.J. Persson, Phys. Scr. 38 (1988) 282.
[24] B.N.J. Persson, A. Baratoff, Phys. Rev. 59 (1987) 339.
[25] N. Lorente, M. Persson, Phys. Rev. Lett. 85 (2000) 2997.
[26] N. Mingo, K. Makoshi, Phys. Rev. Lett. 84 (2000) 3694.
[27] H. Ueba, S.G. Tikhodeev, B.N.J. Persson, Chapter 2 in "Current-Driven Phenomena in Nanoelectronics", Pan Stanford Publishing, 2010.
[28] T. Mii, S. Tikhodeev, H. Ueba, Surf. Sci. 502–503 (2002) 26.
[29] T. Mii, S.G. Tikhodeev, H. Ueba, Phys. Rev. B 68 (2003) 205406.
[30] M. Galperin, M.A. Ratner, A. Nitzan, J. Chem. Phys. 121 (2004) 11965.
[31] T. Frederiksen, M. Paulsson, M. Brandbyge, A.-P. Jauho, INELASTICA can be downloaded from, Phys. Rev. B 75 (2007) 205413 https://github.com/tfrederiksen/inelastica.
[32] A. Garcia-Lekue, D. Sanchez-Portal, A. Arnau, T. Frederiksen, Phys. Rev. B 83 (2011) 155417.
[33] M. Paulsson, T. Frederiksen, H. Ueba, N. Lorente, M. Brandbyge, Phys. Rev. Lett. 100 (2008) 226604.
[34] E. Minamitani, R. Arafune, N. Tsukahara, Y. Ohda, S. Watanabe, M. Kawai, H. Ueba, N. Takagi, Phys. Rev. B 93 (2016) 085411.
[35] E. Minamitani, et al., Phys. Rev. B 96 (2017) 155431.
[36] L. Vitali, M.A. Schneider, K. Kern, L. Wirtz, A. Rubio, Phys. Rev. B 69 (2004) 121414.
[37] H. Gawronski, M. Mehlhorn, K. Morgenstern, Science 319 (2008) 930.
[38] M. Schackert, T. Märkl, J. Jandke, M. Hölzer, S. Ostanin, E.K.U. Gross, A. Ernst, W. Wulfhekel, Phys. Rev. Lett. 114 (2015) 047002.
[39] H.J.W. Haug, A.-P. Jauho, Quantum Kinetics in Transport and Optics of Semiconductors, Springer, 2007.
[40] L.J. Lauhon, W. Ho, Phys. Rev. B 60 (1999) R8525.
[41] J. Ahner, D. Mocuta, R.D. Ramsier, J.T. Yates, Phys. Rev. Lett. 79 (1997) 1889.
[42] J. Braun, J. Weckesser, J. Ahner, D. Mocuta, J.T. Yates, C. Wöll, J. Chem. Phys. 108 (1998) 5161.

[43] J.A. Stroscio, M. Persson, S.R. Bare, W. Ho, Phys. Rev. Lett. 54 (1985) 1428.
[44] R. Heid, K.P. Bohnen, Phys. Rep. 387 (2003) 151.
[45] S. Baroni, S. de Gironcoli, A. Dal Corso, P. Giannozzi, Rev. Mod. Phys. 73 (2001) 515.
[46] B.F. Mason, K. McGreer, B.R. Williams, Surf. Sci. 130 (1983) 282.
[47] P. Zeppenfeld, K. Kern, R. David, K. Kuhnke, G. Comsa, Phys. Rev. B 38 (1988) 12329.
[48] A.P. Baddorf, E.W. Plummer, Phys. Rev. Lett. 66 (1991) 2770.
[49] E. Minamitani, R. Arafune, M.Q. Yamamoto, N. Takagi, M. Kawai, Y. Kim, Phys. Rev. B 88 (2013) 224301.
[50] J. Jandke, P. Hlobil, M. Schackert, W. Wulfhekel, J. Schmalian, Phys. Rev. B 93 (2016) 060505.
[51] M. Brandbyge, J.-L. Mozos, P. Ordejón, J. Taylor, K. Stokbro, Phys. Rev. B 65 (2002) 165401.
[52] Y. Meir, N.S. Wingreen, Phys. Rev. Lett. 68 (1992) 2512.
[53] J.M. Soler, E. Artacho, J.D. Gale, A. García, J. Junquera, P. Ordejón, D. Sánchez-Portal, J. Phys.: Condens. Matter 14 (2002) 2745.
[54] N. Papior, N. Lorente, T. Frederiksen, A. García, M. Brandbyge, Comput. Phys. Commun. 212 (2017) 8.
[55] C. Berger, et al., Science 312 (2006) 1191.
[56] A. Bostwick, T. Ohta, T. Seyller, K. Horn, E. Rotenberg, Nat. Phys. 3 (2007) 36.
[57] K.V. Emtsev, et al., Nat. Mater. 8 (2009) 203.
[58] I. Forbeaux, J.M. Themlin, J.M. Debever, Phys. Rev. B 58 (1998) 16396.
[59] T. Ohta, A. Bostwick, T. Seyller, K. Horn, E. Rotenberg, Science 313 (2006) 951.
[60] A. Tzalenchuk, et al., Nat Nano 5 (2010) 186.
[61] J. Jobst, D. Waldmann, F. Speck, R. Hirner, D.K. Maude, T. Seyller, H.B. Weber, Phys. Rev. B 81 (2010) 195434.
[62] N. Ray, S. Shallcross, S. Hensel, O. Pankratov, Phys. Rev. B 86 (2012) 125426.
[63] J.L. Tedesco, et al., Appl. Phys. Lett. 95 (2009) 122102.
[64] P. Mallet, F. Varchon, C. Naud, L. Magaud, C. Berger, J.Y. Veuillen, Phys. Rev. B 76 (2007) 041403.
[65] C. Riedl, C. Coletti, T. Iwasaki, A.A. Zakharov, U. Starke, Phys. Rev. Lett. 103 (2009) 246804.
[66] F. Varchon, et al., Phys. Rev. Lett. 99 (2007) 126805.
[67] M. Kajihara, T. Suzuki, S.M.F. Shahed, T. Komeda, E. Minamitani, S. Watanabe, Surf. Sci. 647 (2016) 39.
[68] S. Kim, J. Ihm, H.J. Choi, Y.-W. Son, Phys. Rev. Lett. 100 (2008) 176802.
[69] A. Mattausch, O. Pankratov, Phys. Rev. Lett. 99 (2007) 076802.
[70] G.M. Rutter, J.N. Crain, N.P. Guisinger, T. Li, P.N. First, J.A. Stroscio, Science 317 (2007) 219.
[71] G.M. Rutter, N.P. Guisinger, J.N. Crain, E.A.A. Jarvis, M.D. Stiles, T. Li, P.N. First, J.A. Stroscio, Phys. Rev. B 76 (2007) 235416.
[72] T. Seyller, et al., Surf. Sci. 600 (2006) 3906.
[73] F. Fromm, J.M.H. Oliveira, A. Molina-Sánchez, M. Hundhausen, J.M.J. Lopes, H. Riechert, L. Wirtz, T. Seyller, New J. Phys. 15 (2013) 043031.
[74] S. Fratini, F. Guinea, Phys. Rev. B 77 (2008) 195415.
[75] R.J. Koch, S. Fryska, M. Ostler, M. Endlich, F. Speck, T. Hänsel, J.A. Schaefer, T. Seyller, Phys. Rev. Lett. 116 (2016) 106802.
[76] J. Červenka, K. van de Ruit, C.F.J. Flipse, Phys. Rev. B 81 (2010) 205403.
[77] N. Marzari, A.A. Mostofi, J.R. Yates, I. Souza, D. Vanderbilt, Rev. Mod. Phys. 84 (2012) 1419.
[78] F. Giustino, Rev. Mod. Phys. 89 (2017) 015003.
[79] M. Gao, Q.-Z. Li, X.-W. Yan, J. Wang, Phys. Rev. B 95 (2017) 024505.
[80] E.R. Margine, F. Giustino, Phys. Rev. B 87 (2013) 024505.
[81] E.R. Margine, H. Lambert, F. Giustino, Sci. Rep. 6 (2016) 21414.
[82] N.H. Shimada, E. Minamitani, S. Watanabe, Appl. Phys. Express 10 (2017) 093101.
[83] Z. Jun-Jie, D. Shuai, 2D Materials 3 (2016) 035006.
[84] J.P. Perdew, K. Burke, M. Ernzerhof, Phys. Rev. Lett. 77 (1996) 3865.
[85] G. Paolo, et al., J. Phys.: Condens. Matter 21 (2009) 395502.
[86] P.E. Blöchl, O. Jepsen, O.K. Andersen, Phys. Rev. B 49 (1994) 16223.
[87] K. Momma, F. Izumi, J. Appl. Crystallogr. 44 (2011) 1272.
[88] G. Kresse, J. Furthmüller, Phys. Rev. B 54 (1996) 11169.
[89] G. Kresse, J. Furthmüller, Comput. Mater. Sci. 6 (1996) 15.
[90] P.E. Blöchl, Phys. Rev. B 50 (1994) 17953.